DOI: 10.13009/EUCASS2025-276
11TH EUROPEAN CONFERENCE FOR AERONAUTICS AND SPACE SCIENCES (EUCASS)

Aerodynamic Investigation of Seamless and Discrete Camber-Morphed Flaps: A CFD Study for High-Lift Flight

Ravi Kumar[⋆†]*, Santanu Ghosh*[⋆] *and Joel George M*[⋆]
Indian Institute of Technology Madras, Chennai, Tamil Nadu, India
ae20d006@smail.iitm.ac.in · sghosh1@smail.iitm.ac.in · joel@smail.iitm.ac.in
[†]Corresponding author

Abstract

Two- and three-dimensional simulations of subsonic flow over a low-drag NACA 64_1-612 wing were carried out to assess the aerodynamic benefits of a spanwise seamless smooth camber-morphed flap, relative to both spanwise discontinuous smooth camber-morphed and conventional hinged flaps. Reynolds-Averaged Navier-Stokes computations were performed using ANSYS Fluent with Menter's SST $k-\omega$ turbulence model, coupled with a local-correlation-based one-equation γ-transition model. The simulations represent typical flight conditions—takeoff, landing, and maneuvering—for an Unmanned Aerial Vehicle, at *Re* of 1×10^6 and 4.58×10^6. Flap deflections of 10° and 15° were analyzed to generate the high lift demanded during these flight phases. Results show that the seamless smooth camber-morphed flap configuration offers improved aerodynamic efficiency by removing the spanwise gap between the flap and main wing, thus minimizing flap-tip vortex formation and the resulting drag, establishing seamless configuration as the most aerodynamically advantageous mechanism among the designs studied.

1. Introduction

The concept of wing morphing in aerodynamics has drawn inspiration from the natural flight of birds and insects, which adapt their wing shapes across various flight conditions. Broadly, morphing in airplanes can be categorized into three types: in-plane morphing, which alters the wing planform area through span- or chord-wise adjustments; out-of-plane morphing, involving span-wise bending and twisting to control aerodynamic forces; and airfoil morphing, which modifies the camber to improve lift generation by deflecting the trailing edge.

Numerous studies have explored morphing techniques to improve aerodynamic performance. Among these, smooth camber morphing has gained interest as a potential alternative to conventional hinged flaps. Woods and Friswell [1] introduced the Fishbone Active Camber (FishBAC) and showed that it significantly outperforms hinged-flap airfoils in terms of lift and drag. Further optimization by Woods et al. [2] demonstrated FishBAC's effectiveness across various flight conditions. Similarly, Spillman [3] showed that variable camber flaps could reduce cruise drag by up to 23%.

Jo and Majid [4], using the RQ-7a Shadow UAV, demonstrated range and endurance improvements of up to 60% using morphing wings. Other works [5, 6, 7] have confirmed performance gains through camber morphing, particularly in reducing flow separation and improving lift across multiple flight regimes. However, traditional morphing and hinged flap systems typically introduce span-wise gaps between the rigid wing and the flap tips, leading to flow leakage, increased drag, and acoustic penalties [8]. Addressing this, NASA Langley [9] developed a compliant elastomer wedge to seal these gaps. FlexSys Inc. [10] proposed a seamless transition concept integrated with their FlexFoil technology. Woods et al. [11] analyzed a seamless-transition morphing flap for a NACA 0012 wing and showed improved lift and drag characteristics through CFD simulations, although a comparison with discontinuous systems was not presented.

In this study, a three-dimensional CFD analysis of a NACA 64_1-612 rectangular wing equipped with a smooth camber-morphed flap featuring a spanwise seamless transition was performed. This research, compared against configurations with spanwise-discontinuous smooth camber and hinged flaps, provides practical insights into the potential of morphing technology. Simulations are conducted at Reynolds numbers of 1×10^6 and 4.58×10^6, representative of UAV take-off and maneuvering conditions.

Copyright © 2025 by Ravi et al. Published by the EUCASS association with permission.

DOI: 10.13009/EUCASS2025-276

2. Methodology

2.1 Wing cross-section and flap profile

For this study, NACA 64_1-612 airfoil was selected because of its excellent aerodynamic characteristics, particularly for UAVs. Belonging to the NACA 6-series, this airfoil is specifically designed for low-drag over a wide spectrum of lift coefficients, especially at moderate to high Reynolds numbers. This inherent characteristic makes it highly suitable for both takeoff/landing and maneuvering flights. A significant amount of experimental data for this airfoil exists across diverse Reynolds numbers, as thoroughly documented by Loftin and Smith [12], enabling good comparison and validation for the computational findings. The baseline airfoil coordinates were taken from [12], whereas the hinged flap (HF) profile was developed based on the approach described by Jawahar et al. [13].

The smooth camber-morphed flap (SCMF) trailing edge geometry spanning from 0.7c to 0.9c as shown in Fig. 1, was generated based on the approach proposed by Daynes and Weaver [14]. The vertical displacement profile of the camber-morphed TE is represented by a third-order polynomial given in Eq. (1) and Eq. (2), expressed as:

$$w(x) = \phi(x)\sin(\delta) \tag{1}$$

$$\phi(x) = \begin{cases} 0, & 0 \le x < c - c_f \\ \dfrac{(c - x - c_f)^3}{c_f^2}, & c - c_f \le x \le c \end{cases} \tag{2}$$

and the expressions describing the upper and lower surfaces of the smooth camber-morphed flap are given in Eq. (3) and Eq. (4).

$$y_{u,c}(x) = y_{u,b}(x) + w(x) \tag{3}$$

$$y_{l,c}(x) = y_{l,b}(x) + w(x) \tag{4}$$

where,

$w(x)$ = Expression governing surface camber-morphing
$y_{u,b}(x)$ = Expression of the upper surface of the baseline airfoil
$y_{l,b}(x)$ = Expression of the lower surface of the baseline airfoil
$y_{u,c}(x)$ = Expression of the upper surface of the camber-morphed airfoil
$y_{l,c}(x)$ = Equation of the lower surface of the camber-morphed airfoil
δ = Flap-deflection angle (deg)
x = Chord-wise position (m)
c_f = Trailing-edge-flap length (m)
c = Chord length (m)

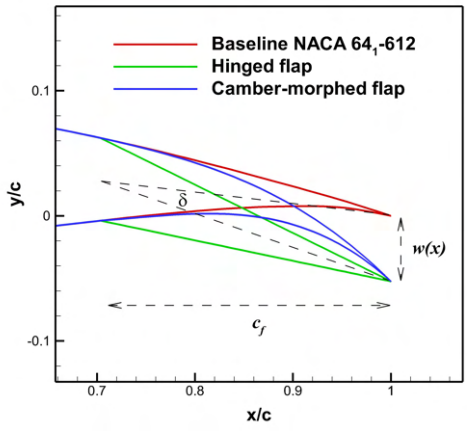


Figure 1: Baseline, hinged, and smooth camber-morphed flap profiles for NACA 64_1-612 airfoil

DOI: 10.13009/EUCASS2025-276

2.2 Seamless-transition wing model

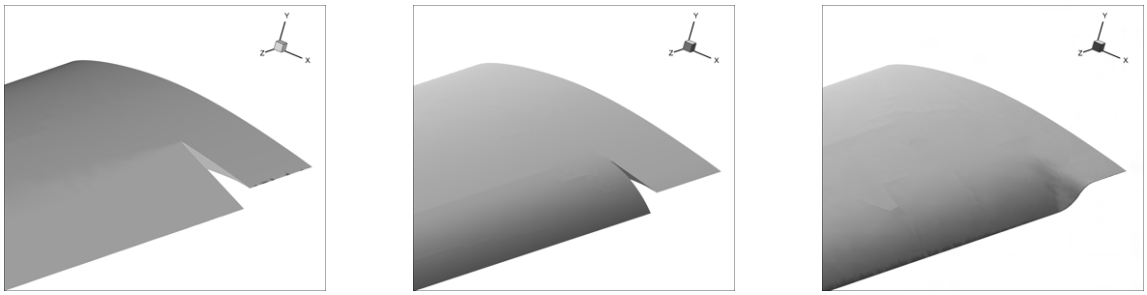
A rectangular wing with an aspect ratio of fifteen was considered with flap variants including the hinged flap (HF) wing, the smooth camber-morphed flap (SCMF) wing, and the seamless-transition smooth camber-morphed flap (S-SCMF) wing, as shown in Fig. 2. In all configurations, the flap spanned a (spanwise) portion of the wing, keeping a small clearance near the wing root. In the S-SCMF design, the flap connected smoothly into the main wing over a spanwise transition region, with the transition length entirely taken from the flap width, as shown in Fig. 3a.

The trailing edge coordinates of the S-SCMF wing within the transition region, shown for various flap deflection angles in Fig. 3b, were determined using the trigonometric shape function given in Eq. (5), as proposed by Woods et al. [11].

$$w(z) = h\cos\left(\frac{\pi z}{l}\right) - h\,, \qquad 0 \le z \le 0.25 \tag{5}$$

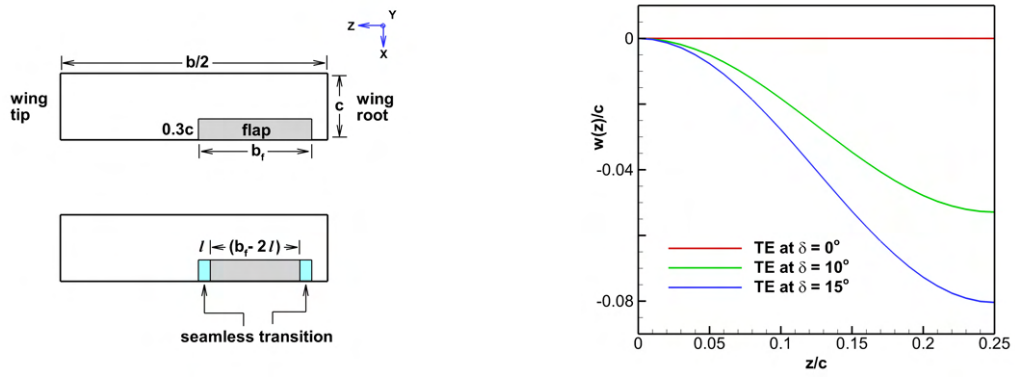
where

$w(z)$ = Vertical displacement of the trailing-edge (m)
z = Spanwise distance along the transition (m)
h = Half-amplitude of the control surface deflection (m)
l = Spanwise length of the morphing portion of the transition (m)



(a) HF (b) SCMF (c) Seamless SCMF

Figure 2: 3D models of (a) Hinged flap wing, (b) Smooth camber-morphed flap wing, and (c) Seamless-transition smooth camber-morphed flap wing



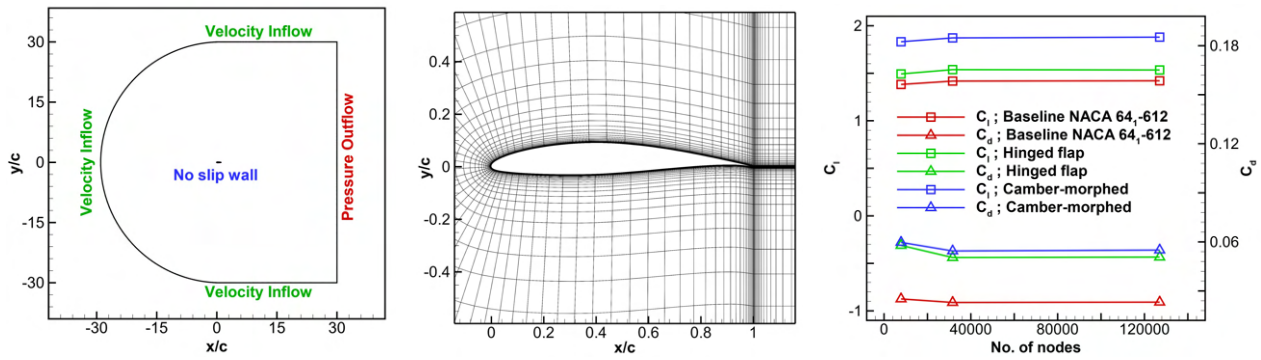
(a) (b)

Figure 3: (a) Schematic of non-seamless vs. seamless-transition rectangular flap wings, and (b) Spanwise variation of the trailing-edge vertical displacement in the transition region of seamless flap for $\delta = 0°$, 10°, and 15°

DOI: 10.13009/EUCASS2025-276

2.3 Computational details and grid convergence

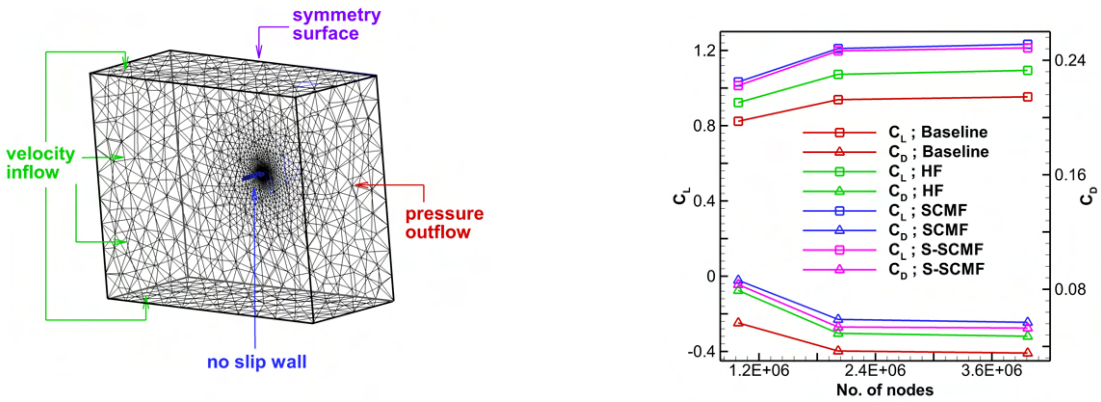
CFD investigations were performed using Reynolds-Averaged Navier-Stokes (RANS) simulations in ANSYS Fluent. These simulations employed a steady-state, pressure-based solver, and the SST k–ω two-equation turbulence model. A local correlation-based γ-transition model was also used. For spatial discretization of the momentum equations, a least-squares cell-based gradient method was used for viscous fluxes and second-order upwind method was used for inviscid fluxes, while a first-order upwind scheme was applied to the turbulent kinetic energy and specific dissipation rate equations. For 2D simulations, a C-type computational domain was used, with its configuration and boundary conditions shown in Fig. 4a. To adequately capture near-wall flow phenomena, the wall-normal grid was expanded to ensure y^+ values remained below 1 in the first cell layer adjacent to the wing's surface (Fig. 4b). Further grid refinement was applied near the leading and trailing edges to precisely resolve flow gradients. For visual clarity in Fig. 4b, some grid lines were omitted in both streamwise and transverse directions. A grid independence study was carried out through an evaluation of meshes spanning from 7,830 to 127,020 nodes. Ultimately, a structured grid containing 31,600 nodes was chosen after assessing its impact on lift and drag predictions (Fig. 4c).



(a) (b) (c)

Figure 4: (a) C-type fluid domain with boundary conditions, (b) Structured grid all around the airfoil, and (c) 2D grid convergence test results.

3D simulations were performed using a cuboidal computational domain featuring a hybrid mesh. A structured mesh was generated near the wing surface, transitioning to an unstructured mesh in the far-field region (Fig. 5a). Boundary conditions included velocity inlet, pressure outlet, symmetry planes, and no-slip walls (Fig. 5a). Grid sensitivity studies involved meshes ranging from 986,457 to 3,968,925 nodes; a mesh with 2,015,416 nodes was selected based on its ability to accurately predict aerodynamic performance (Fig. 5b).



(a) (b)

Figure 5: (a) Hybrid mesh (structured mesh near NACA 64$_1$-612 airfoil wing surface and unstructured mesh in the far-field) with boundary conditions, (b) 3D grid convergence test results.

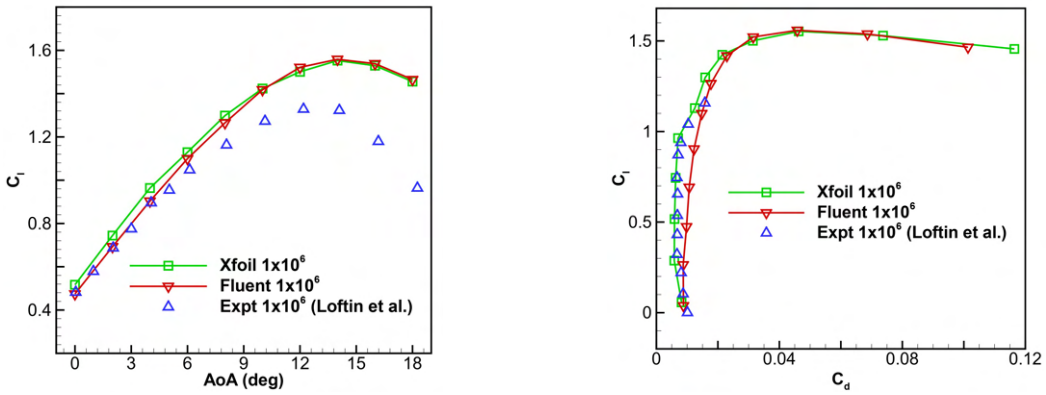
DOI: 10.13009/EUCASS2025-276

3. Results & Discussion

This section presents the computational results obtained from the aerodynamic analysis of different flap configurations: the smooth camber-morphed discontinuous flap wing, smooth camber-morphed seamless flap wing, and conventional (discontinuous) hinged flap wing. The aerodynamic performance of these configurations is assessed in terms of lift, drag, and pressure distribution for different angles of attack, focusing on the take-off and maneuvering flight stages of a UAV.

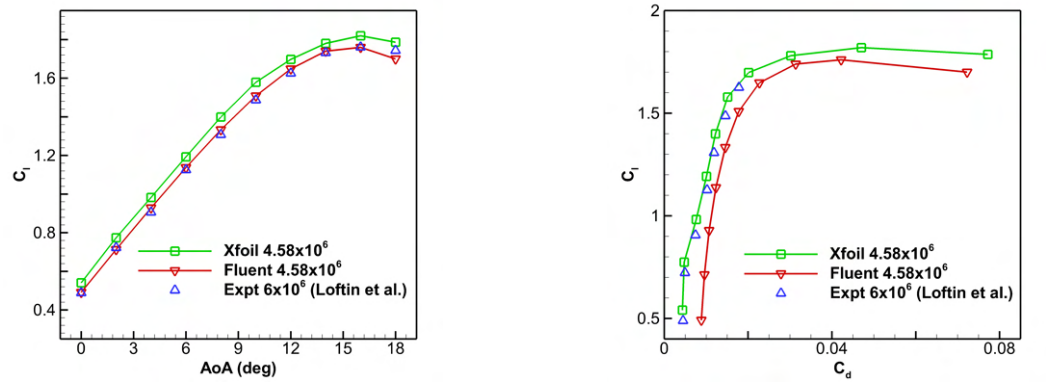
3.1 Validation

For validation, NACA 64_1-612 airfoil of chord length 1 m is considered for calculating the 2D aerodynamic characteristics for take-off ($Re = 1\times10^6$) and maneuvering ($Re = 4.58\times10^6$) flight stages of a UAV. CFD predictions from Fluent are compared with data available from literature [Loftin and Smith [12]] and Xfoil predictions in Figs. 6 and 7. It is observed that while the lift predictions by Fluent have excellent agreement with experimental data at $Re = 4.58\times10^6$, the comparison is good only for low-to-moderate angles of attack ($0° - 6°$) at the lower Re of 1×10^6. It is worthwhile to note that at $Re = 1\times10^6$, the c_l vs. AoA curve shows linear behavior for the same range of AoA. Further, Xfoil tends to over-predict lift for both the Re. As far as drag predictions are considered, Xfoil predictions show closer agreement with the experimental data, compared to the RANS CFD predictions [15, 16, 17, 18]. Experimental data at $Re = 6\times10^6$ are used due to the unavailability of data at the target $Re = 4.58\times10^6$, as it was the closest available experimental dataset. It is also worth noting that as Re increases, drag tends to decrease, which is reflected in the drag polar plot shown in Fig. 7.



(a) (b)

Figure 6: (a) c_l vs. AoA (deg), and (b) c_l vs. c_d at Re : 1×10^6



(*a*) (*b*)

Figure 7: (a) c_l vs. AoA (deg), and (b) c_l vs. c_d at Re : 4.58×10^6

DOI: 10.13009/EUCASS2025-276

3.2 Airfoil and wing analysis

In this section, the two-dimensional aerodynamic results are first presented and analyzed in detail for two different Reynolds number, $Re = 1 \times 10^6$ and 4.58×10^6, and two downward flap deflections, $\delta = 10°$ and $15°$, which are representative of typical conditions encountered during UAV take-off/landing and maneuvering respectively. This detailed analysis aims to provide a clear understanding of the aerodynamic behavior and performance of the HF and SCMF configurations for a wing section. The comparative assessment focuses on the impact of Re and δ on lift (c_l), drag (c_d), and overall aerodynamic efficiency (c_l/c_d) for each configuration. This is followed by a comparative study conducted to evaluate and contrast the aerodynamic characteristics of the three-dimensional HF, SCMF, and S-SCMF configurations of a rectangular wing to ascertain whether any aerodynamic advantage is offered by the S-SCMF configuration over the HF and SCMF configurations. Further, flow phenomena such as wing-tip vortices, flap-tip vortices, and spanwise pressure gradients, which cannot be captured in two-dimensional airfoil studies, are also compared for the different wing-flap configurations.

3.2.1 Aerodynamic performance analysis of airfoils with different flap configurations

Fig. 8 presents the variation of the airfoil lift coefficient (c_l) with angle of attack (AoA) for different flap configurations at two Re (1×10^6 and 4.58×10^6) and two downward flap deflections ($10°$ and $15°$). The SCMF airfoil shows a significant increase in c_l compared to the HF and baseline airfoil across all AoAs. This improvement is attributed to the smooth surface geometry change at the starting location of the flap, which ensures flow attachment (Figs. 13 and 14) and gradual pressure recovery (Fig. 12), thereby extending the favorable pressure gradient region along the streamwise direction. However, the SCMF airfoil experiences stall earlier than the HF configuration.

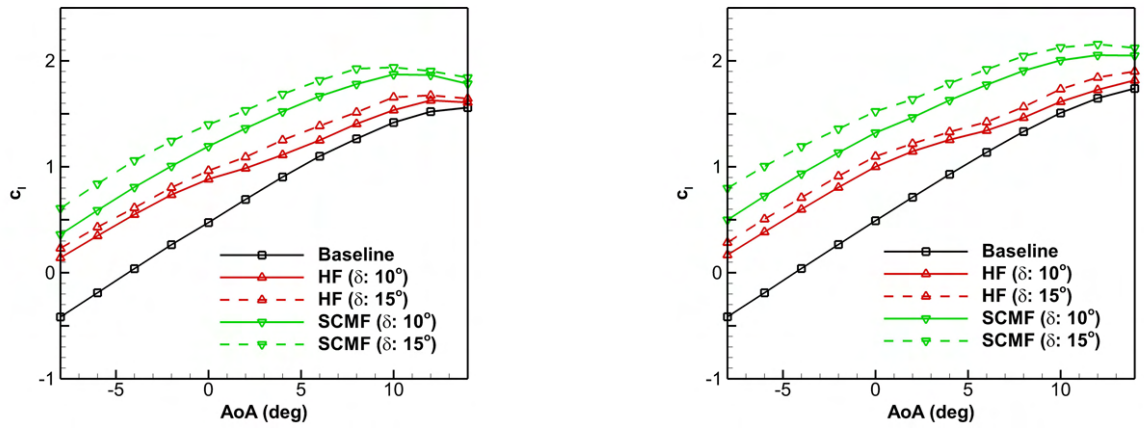
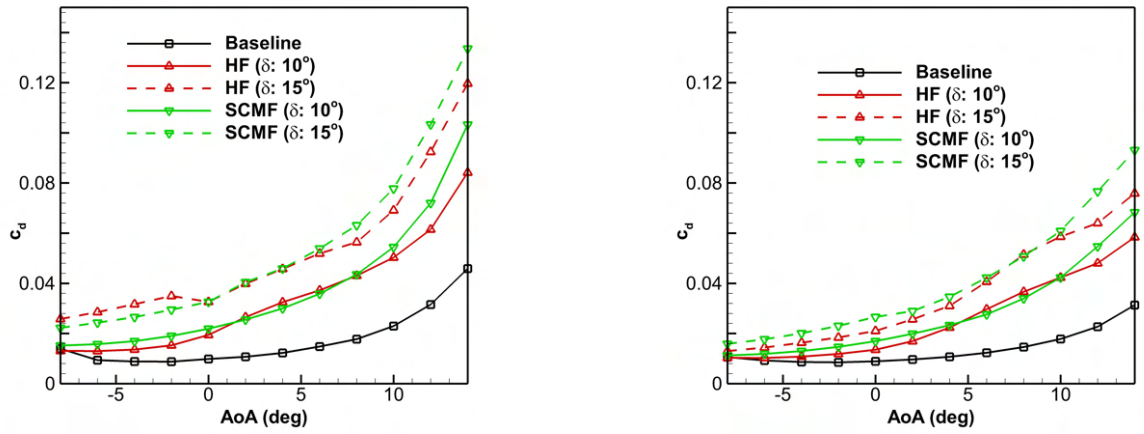


Figure 8: c_l vs. AoA (deg) plots for (a) Re : 1×10^6 and (b) 4.58×10^6

Fig. 8 also shows that the c_l increases for all airfoil configurations, including the baseline, with increasing Re and flap deflection. While the increase of lift (for any AoA) with flap-deflection is expected, as it effectively increases the camber of the airfoil, the higher lift obtained with the increase in Re has been reported in literature previously [19, 20]. As observed for the baseline airfoil in Figs. 6 and 7, the stall angle also reduces with increase in Re for the HF and SCMF configurations.

The drag coefficient (c_d) variation is shown in Fig. 9, which indicates that the c_d produced by the SCMF airfoil is generally higher than that of the HF airfoil across most AoAs for a given flap deflection. However, an interesting observation is that within the typical take-off AoA range of the UAV, the SCMF airfoil generates lower drag than the HF airfoil. As the flap deflection increases, c_d increases for both airfoil configurations due to the higher camber and increased pressure drag caused by larger deflection angles. Another notable observation is that with increasing Reynolds number (Re), drag coefficient (c_d) decreases significantly, with an average reduction of nearly 25%. This reduction occurs because higher Re enhances the boundary layer's ability to resist flow separation (Figs. 13 and 14), which reduces pressure drag caused by flow separation. Additionally, the decrease in skin friction drag coefficient with increasing Re may also contribute to this effect.

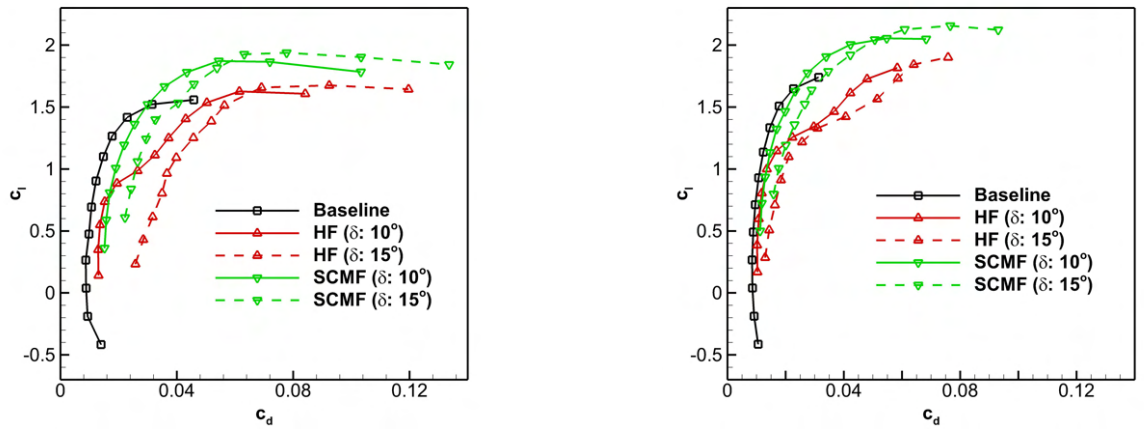
DOI: 10.13009/EUCASS2025-276



(a) (b)

Figure 9: c_d vs. AoA (deg) plots for (a) Re : 1×10^6 and (b) 4.58×10^6

The drag polar (c_l vs. c_d) presented in Fig. 10 shows that for certain c_l values ($\geq$ 1.2, which is typical for UAV take-off), the SCMF airfoil generates significantly lower drag compared to the HF airfoil. Also, the maximum achievable c_l is higher with SMCF compared to the HF configuration for both the Re. The maximum achievable c_l is higher with SCMF than HF for both the Re. Additionally, the plots indicate that at the higher Re of 4.58×10^6, all configurations experience lower drag for the same c_l compared to the lower Re (1×10^6) case.

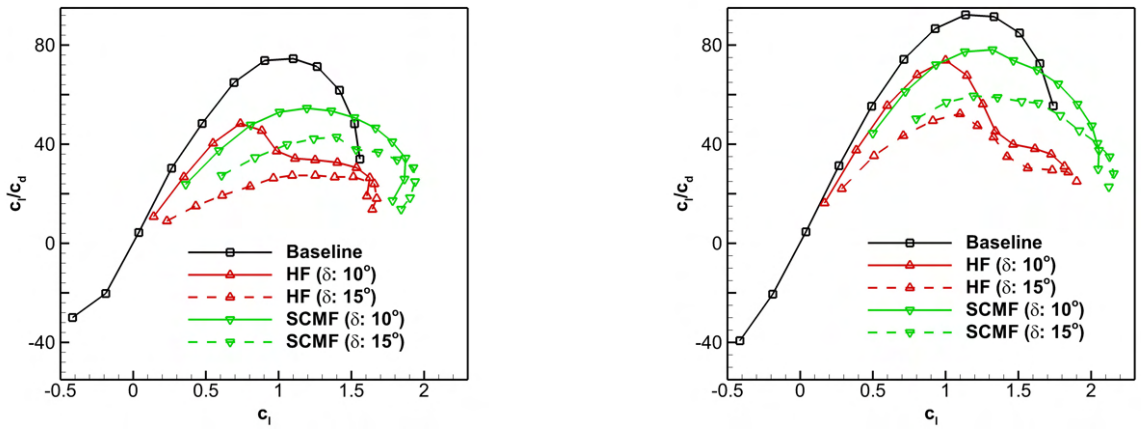


(a) (b)

Figure 10: c_l vs. c_d plots for (a) Re : 1×10^6 and (b) 4.58×10^6

Fig. 11 shows the variation of the lift-to-drag ratio (c_l/c_d) with the lift coefficient (c_l) for the two values of Re investigated herein: 1×10^6 and 4.58×10^6. SCMF airfoil consistently achieves higher c_l/c_d compared to the HF airfoil for the $c_l > 1.1$, highlighting the aerodynamic efficiency gained from the smooth, continuous camber variation for both the flap deflections (10° and 15°). The plots also indicate that an increase in Re improves the c_l/c_d for all airfoil configurations.

DOI: 10.13009/EUCASS2025-276

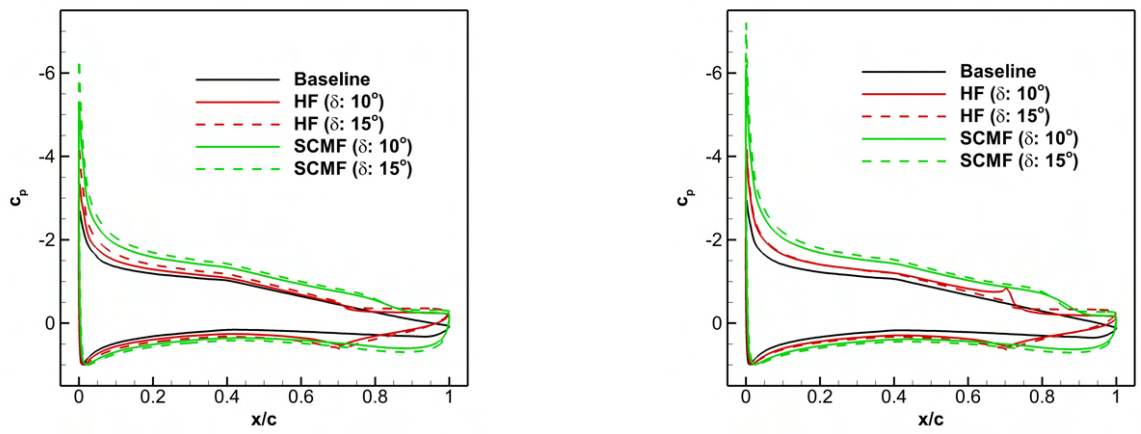


(a) (b)

Figure 11: c_l/c_d vs. c_l plots for (a) Re : 1×10^6 and (b) 4.58×10^6

3.2.2 Airfoil surface pressure distribution and flow analysis

The c_p distribution plots presented in Fig. 12 for an AoA of 6° provide insight into the enhanced lift generation achieved with the SCMF configuration. The plots reveal that, for the airfoil section immediately downstream of the starting location of the flap ($x/c > 0.7$), the SCMF exhibits higher c_p values on the pressure surface and lower values on the suction surface compared to the HF. This increased difference in c_p values between the suction and pressure surface c_p values leads to greater lift generation, indicating that the SCMF is more effective at enhancing lift than the HF. With increasing flap deflection, the difference between the suction and pressure surface c_p values increases for both HF and SCMF configurations, thereby enhancing lift. Furthermore, in the HF case, the pressure rise is more abrupt and occurs closer to the hinged location, resulting in the formation of a larger separation bubble compared to the SCMF. This trend is observed for both flap deflections (10° and 15°), as shown later in Figs. 13 and 14.

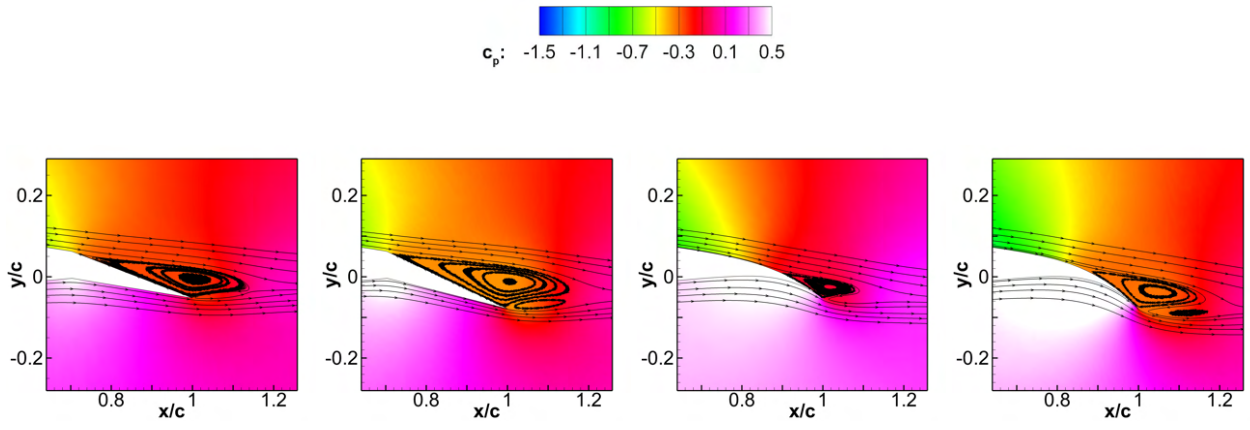


(a) (b)

Figure 12: c_p vs. x/c plots for (a) Re: 1×10^6 and (b) 4.58×10^6 at AoA: 6°

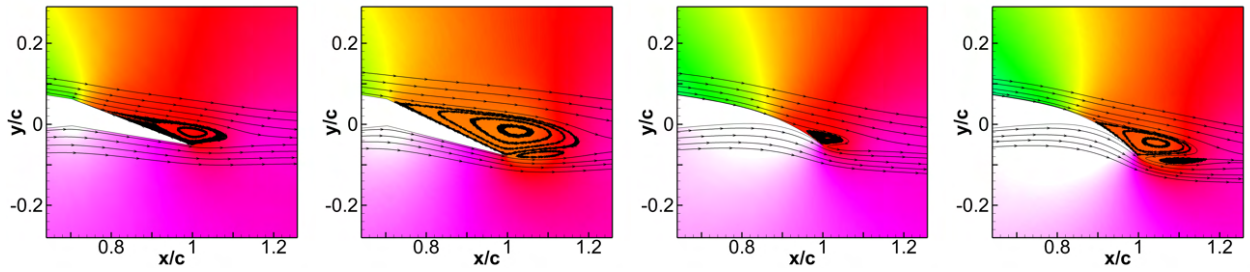
Additionally, increasing Re increases the difference between the suction and pressure surface c_p values, leading to higher lift generation. Higher Re shifts the sharp rise in the unfavorable pressure gradient further downstream along the airfoil, leading to a smaller separation bubble and, consequently, a reduction in aerodynamic drag (Figs. 13 and 14).

DOI: 10.13009/EUCASS2025-276



(a) HF (δ : 10°) (b) HF (δ : 15°) (c) SCMF (δ : 10°) (d) SCMF (δ : 15°)

Figure 13: c_p contour plots with streamlines of hinged flaps (HF) and smooth cambered morph flaps (SCMF) for AoA: 6° at Re : 1×10^6



(a) HF (δ : 10°) (b) HF (δ : 15°) (c) SCMF (δ : 10°) (d) SCMF (δ : 15°)

Figure 14: c_p contour plots with streamlines of hinged flaps (HF) and smooth cambered morph flaps (SCMF) for AoA: 6° at Re : 4.58×10^6

3.2.3 Aerodynamic performance analysis of wings with different flap configurations

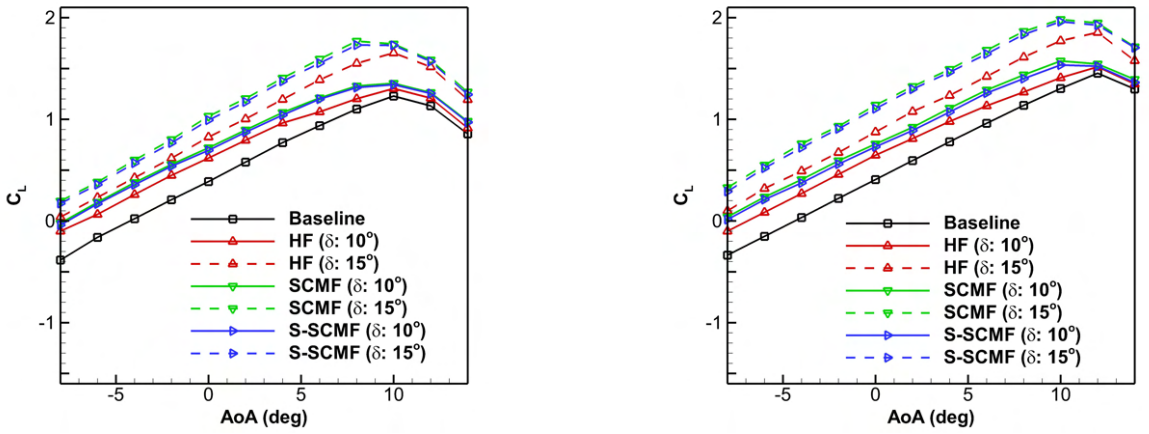
Fig. 15 illustrates the variation of the lift coefficient (C_L) with respect to the angle of attack (AoA) for various flap wing designs: hinged flap (HF), smooth camber-morphed flap (SCMF), and seamless-transition smooth camber-morphed flap (S-SCMF), evaluated at two distinct flap deflections and Re. Prior investigations at the airfoil level [19] indicated that the SCMF arrangement yields considerably greater lift compared to the HF for identical flap deflections. This trend is consistent at the wing level as well.

Nevertheless, 3D analysis demonstrated that the S-SCMF wing exhibits marginally reduced lift relative to the SCMF wing throughout the AoA range. This decrease is linked to the shorter spanwise flap length in the S-SCMF configuration, designed to enable a seamless spanwise transition between the flap and the main wing. Furthermore, an increase in flap deflection angle (δ) and Re results in higher lift for all flap-wing types. It was also found that while δ does not impact the stall angle but the stall angle tends to increase with Re.

The variation of drag coefficient (C_D) with angle of attack (AoA) is illustrated in Fig. 16. It is evident that the drag produced by the SCMF wing remains higher than that of the HF wing throughout the entire range of AoA. This increase in drag can be linked to the enhanced surface curvature and the resulting pressure differential between the upper and lower surfaces near the trailing edge, caused by the smooth camber-morphing mechanism. While this mechanism improves lift, it also leads to an increase in pressure drag. Nevertheless, the seamless-transition SCMF (S-SCMF) configuration demonstrates a marginally reduced drag in comparison to the SCMF configuration. This decrease primarily results from the elimination of the spanwise gap separating the main wing section from the smooth camber-morphed flap. The removal of this gap weakens the flap-tip vortices, thereby lowering the induced drag associated with these vortices.

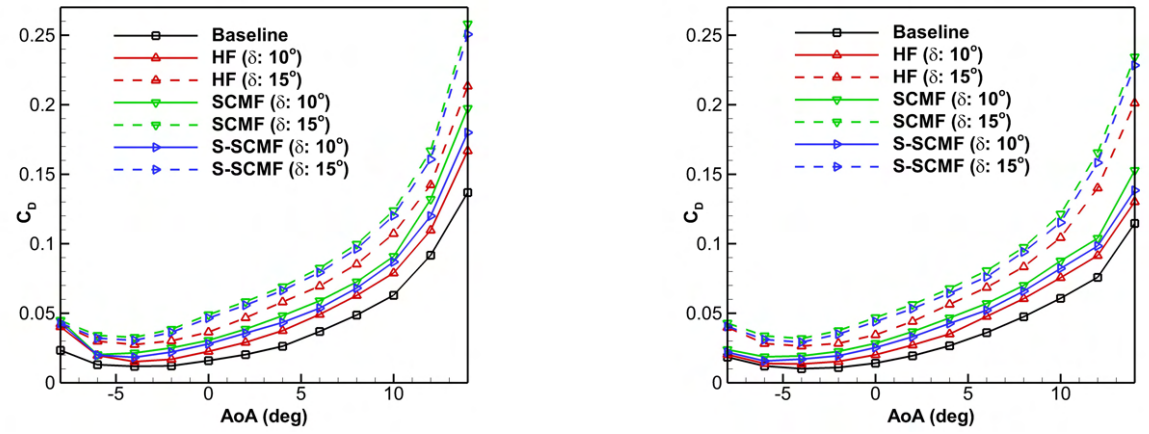
The drag polar plots (C_L vs. C_D) illustrated in Figs. 17 and 18 enable a more precise assessment of the aerodynamic efficiency across various flap-wing configurations. As evident from Fig. 18, the S-SCMF setup achieves the

DOI: 10.13009/EUCASS2025-276



(a) (b)

Figure 15: C_L vs. AoA (deg) plots for (a) Re: 1×10^6 and (b) 4.58×10^6

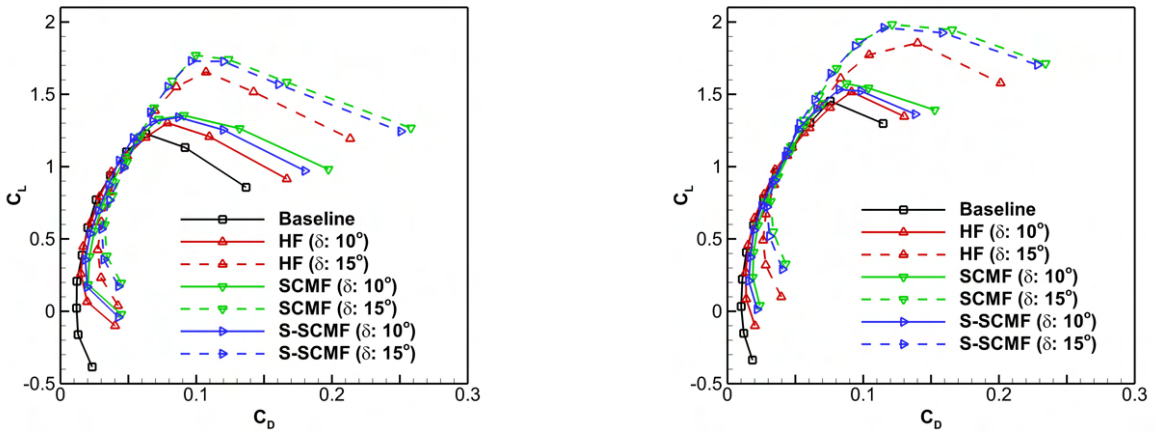


(a) (b)

Figure 16: C_D vs. AoA (deg) plots for (a) Re: 1×10^6 and (b) 4.58×10^6

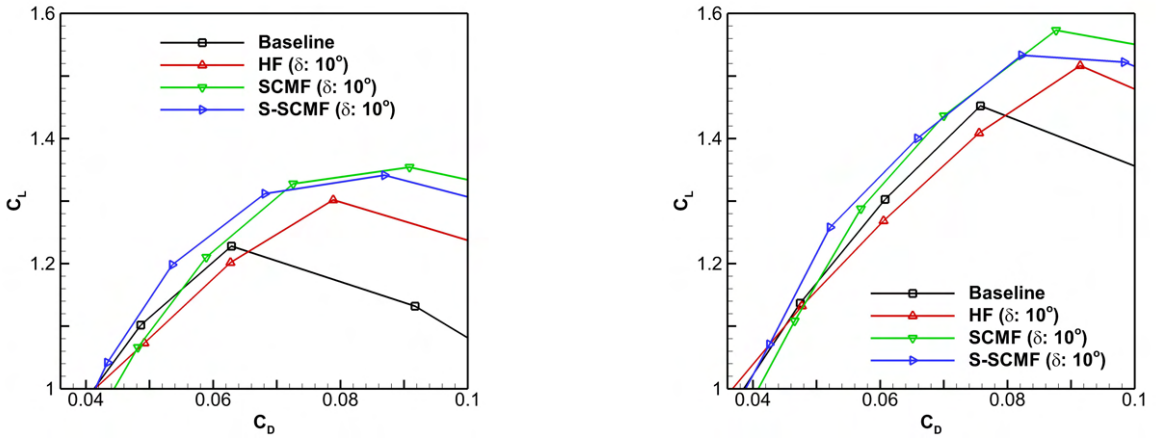
lowest C_D for a specified C_L within the higher lift range of 1.1 to 1.3, across both *Re* considered in this study. This confirms that the spanwise-seamless transition of the S-SCMF wing effectively reduces the drag penalty while enhancing lift generation and improving overall aerodynamic efficiency.

DOI: 10.13009/EUCASS2025-276



(a) (b)

Figure 17: C_L vs. C_D plots for (a) Re: 1×10^6 and (b) 4.58×10^6

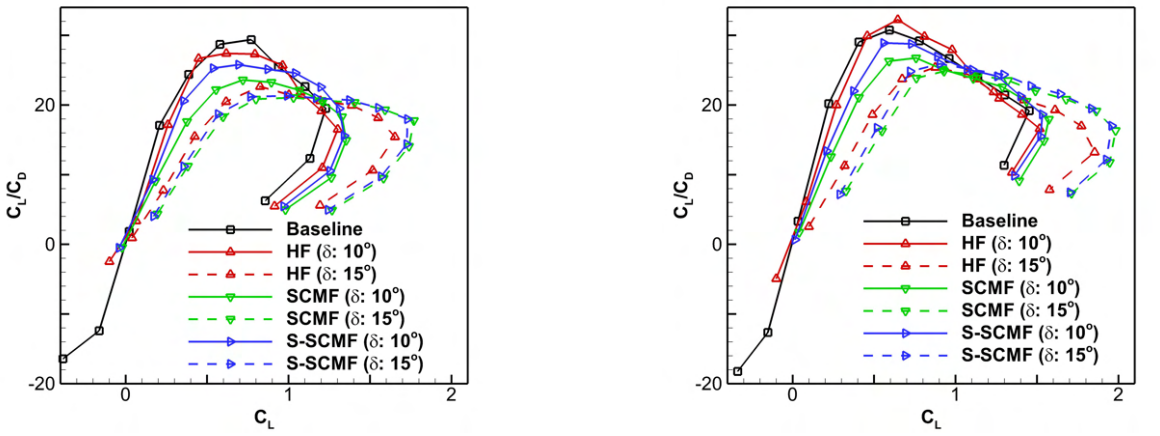


(a) (b)

Figure 18: Zoomed viewed of C_L vs. C_D plots for (a) Re: 1×10^6 and (b) 4.58×10^6

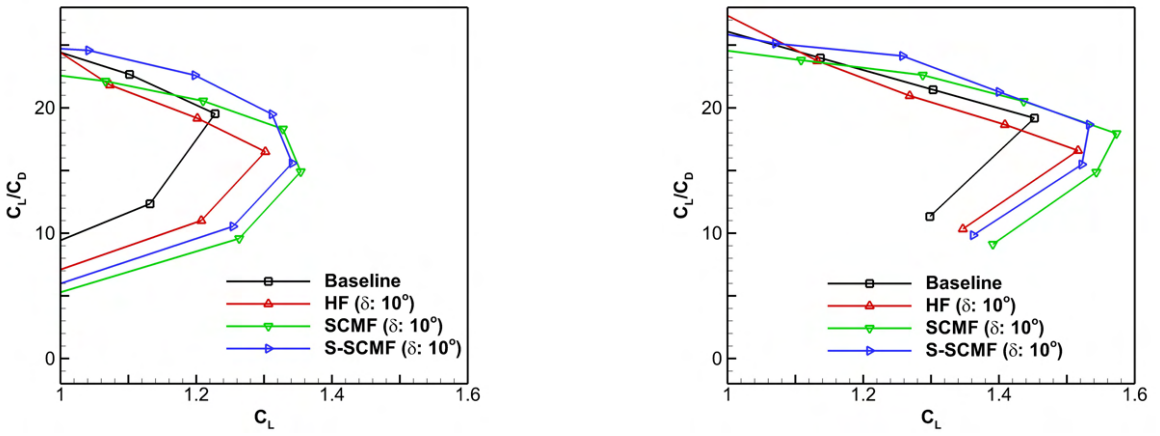
Figs. 19 and 20 shows the variation of lift-to-drag ratio (C_L/C_D) with lift coefficient (C_L) for various flap wing configurations at *Re* of 1×10^6 and 4.58×10^6. When C_L exceeds 1.1, indicating the regime where flap effectiveness becomes critical, the S-SCMF configuration consistently outperforms the other two configurations.

DOI: 10.13009/EUCASS2025-276



(a) (b)

Figure 19: C_L/C_D vs. C_L plots for (a) Re: 1×10^6 and (b) 4.58×10^6



(a) (b)

Figure 20: Zoomed view of C_L/C_D vs. C_L plots for (a) Re: 1×10^6 and (b) 4.58×10^6

3.2.4 Wing Surface pressure distribution and flow analysis

Fig. 21 shows the streamlines, surface pressure coefficient (c_p), and normalized streamwise x-vorticity (Ω_x) contours plotted on a crosswise plane for different flapped wing configurations at an angle of attack of 6° and $Re = 1 \times 10^6$. These results correspond to a flap deflection of 10°. The contour plots reveal that in both the spanwise and streamwise directions, the low-pressure region over the wing's upper surface extends more in the SCMF and S-SCMF cases compared to the HF configuration. This extension suggests that the SCMF and S-SCMF wings are capable of generating greater lift than the HF wing. The contours of x-vorticity in the wake region further show how different flap types influence flap-tip vortex characteristics. Among all cases, the SCMF configuration shows the most pronounced vortex core. This observation is consistent with a higher pressure differential between the pressure and suction surfaces along the flap, as also noted in the corresponding airfoil-level studies [19].

DOI: 10.13009/EUCASS2025-276

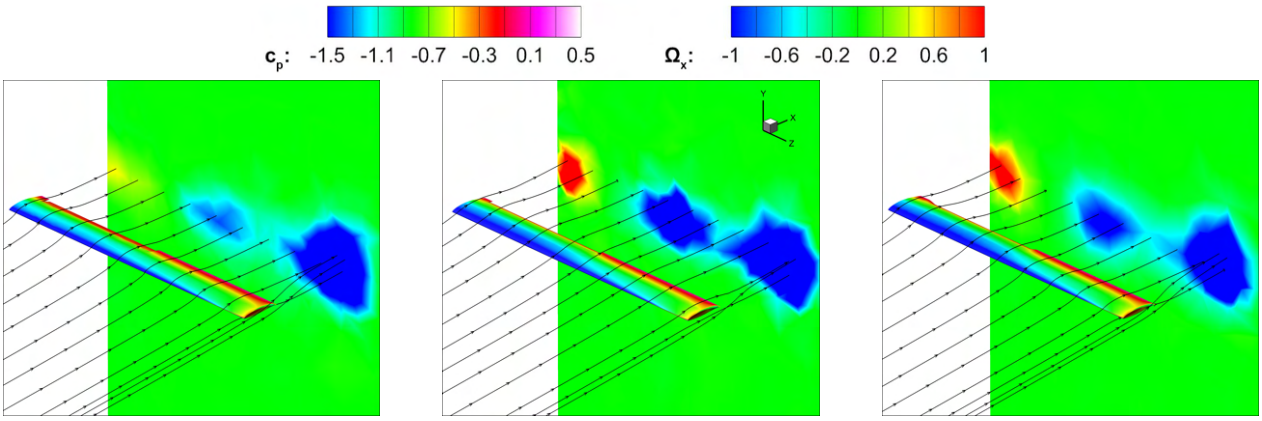


Figure 21: Streamlines with c_p contours on the (a) HF, (b) SCMF, and (c) S-SCMF wing surfaces and normalized x-vorticity contours on a crosswise plane in the wake at AoA of 6°, δ = 10°, and $Re = 1 \times 10^6$

In comparison between S-SCMF and HF wings, both exhibit smaller vortex cores. For the HF configuration, the diminished core strength is primarily due to a reduced pressure differential across the wing surfaces, unlike the smoothly morphed flaps. On the other hand, in the S-SCMF configurations, the reduction in vortex core size is attributed to the seamless connection between the flap and the main wing, which eliminates the spanwise discontinuity typically responsible for initiating the flap-tip vortex.

4. Conclusions

This study aimed to investigate the aerodynamic benefits of using smooth camber morphed flaps in place of conventional hinged flaps for lift augmentation during the take-off/landing and maneuvering flight stages of an Unmanned Aerial Vehicle (UAV). The analysis was conducted for two flap deflections (10° and 15°) and at two Reynolds numbers (1×10^6 and 4.58×10^6). First, two-dimensional airfoil-level analysis was carried out to compare the performance of a smooth camber-morphed flap (SCMF) with a conventional hinged flap (HF). The results demonstrated that the SCMF configuration is aerodynamically more efficient than the HF configuration for both deflections and Reynolds numbers, due to substantially higher lift generation that more than offset any additional drag penalty incurred. The higher lift generation for the smooth morphed flap was caused by larger difference of pressure between the suction and pressure surfaces along the length of the airfoil, and especially along the length of the flap, compared to the hinged-flap.

To determine a more practical estimate of the benefits of smooth camber morphing, simulations of a rectangular wing with the different flap configurations spanning about 30% of the wing were investigated next. Furthermore, a seamless-transition smooth camber-morphed flap (S-SCMF) mechanism was also investigated to evaluate its potential in enhancing lift by reducing flap-tip vortex strength, which otherwise is expected to reduce wing lift and increase induced drag. The results revealed that the S-SCMF design effectively reduces flap-tip vorticity by removing the spanwise gap at the flap tips. The effectiveness of the S-SCMF design in mitigating flap-tip vorticity (thus reducing induced drag) and improve lift generation makes it a more effective mechanism compared to both HF and SCMF configurations. These findings highlight the potential of the S-SCMF design in improving UAV performance during take-off and maneuvering flight phases.

References

[1] Benjamin King Sutton Woods and Michael I Friswell. Preliminary investigation of a Fishbone Active Camber concept. In *Smart Materials, Adaptive Structures and Intelligent Systems*, volume 45103, pages 555–563. American Society of Mechanical Engineers, 2012.

[2] Benjamin King Sutton Woods, James HS Fincham, and Michael I Friswell. Aerodynamic modelling of the Fish Bone Active Camber Morphing concept. In *Proceedings of the RAeS Applied Aerodynamics Conference, Bristol, UK*, volume 2224, 2014.

[3] JJ Spillman. The use of variable camber to reduce drag, weight and costs of transport aircraft. *The Aeronautical Journal*, 96(951):1–9, 1992.

DOI: 10.13009/EUCASS2025-276

[4] Bruce W Jo and Tuba Majid. Enhanced range and endurance evaluation of a camber morphing wing aircraft. *Biomimetics*, 8(1):34, 2023.

[5] A Garcia Naranjo, I Cowling, JA Green, and N Qin. Aerodynamic performance benefits of utilising camber morphing wings for Unmanned Air Vehicles. *The Aeronautical Journal*, 117(1189):315–327, 2013.

[6] R Jini Raj and J Bruce Ralphin Rose. Flow physics and boundary layer optimization over a NACA airfoil by camber morphing at subsonic speeds. *International Journal of Modern Physics C*, 34(06):2350080, 2023.

[7] Thomas A Reist, David Koo, and David W Zingg. Aircraft cruise drag reduction through variable camber using existing control surfaces. *Journal of Aircraft*, 59(6):1406–1415, 2022.

[8] M Macaraeg. Fundamental investigations of airframe noise. In *4th AIAA/CEAS Aeroacoustics Conference*, page 2224, 1998.

[9] Mehdi R Khorrami, David P Lockard, James B Moore, Ji Su, Travis L Turner, John C Lin, Karen M Taminger, Seun K Kahng, Scott A Verden, et al. Elastically deformable side-edge link for trailing-edge flap aeroacoustic noise reduction, April 15 2014. US Patent-8,695,925.

[10] Joel Hetrick, Russell Osborn, Sridhar Kota, Peter Flick, and Donald Paul. Flight testing of mission adaptive compliant wing. In *48th AIAA/ASME/ASCE/AHS/ASC Structures, Structural Dynamics, and Materials Conference*, page 1709, 2007.

[11] Benjamin King Sutton Woods, Laura Parsons, Alexander B Coles, James HS Fincham, and Michael I Friswell. Morphing elastically lofted transition for active camber control surfaces. *Aerospace Science and Technology*, 55: 439–448, 2016.

[12] Laurence K Loftin and Hamilton A Smith. Aerodynamic Characteristics of 15 NACA Airfoil Sections at Seven Reynolds Numbers From 0.7×10^6 To 9.0×10^6, 1949. NACA-TN-1945.

[13] Hasan Kamliya Jawahar, Qing Ai, and Mahdi Azarpeyvand. Experimental and numerical investigation of aerodynamic performance for airfoils with morphed trailing edges. *Renewable Energy*, 127:355–367, 2018.

[14] Stephen Daynes and Paul M Weaver. A morphing trailing edge device for a wind turbine. *Journal of Intelligent Material Systems and Structures*, 23(6):691–701, 2012.

[15] Q Chanzy and AJ Keane. Analysis and experimental validation of morphing UAV wings. *The Aeronautical Journal*, 122(1249):390–408, 2018.

[16] C Thill, JD Downsborough, SJ Lai, IP Bond, and DP Jones. Aerodynamic study of corrugated skins for morphing wing applications. *The Aeronautical Journal*, 114(1154):237–244, 2010.

[17] Rui Wu, Constantinos Soutis, Shan Zhong, and AJ Filippone. A morphing aerofoil with highly controllable aerodynamic performance. *The Aeronautical Journal*, 121(1235):54–72, 2017.

[18] K Dhileep, D Kumar, PN Gautham Vigneswar, P Soni, S Ghosh, S Faruque Ali, and A Arockiarajan. Aerodynamic study of single corrugated variable-camber morphing aerofoil concept. *The Aeronautical Journal*, 126 (1296):316–344, 2022.

[19] Ravi Kumar and Santanu Ghosh. Numerical investigation of the trailing edge morphing using corrugated skin at a high Reynolds Number for NACA 0012 & NACA 64(1)-612 airfoils. In *AIAA AVIATION 2023 Forum*, pages 3–10, Reston, Virginia, 6 2023. American Institute of Aeronautics and Astronautics. ISBN 978-1-62410-704-7.

[20] Justin Winslow, Hikaru Otsuka, Bharath Govindarajan, and Inderjit Chopra. Basic understanding of airfoil characteristics at low Reynolds numbers ($10^4 - 10^5$). *Journal of Aircraft*, 55(3):1050–1061, 2018.